2024 IEEE International Conference on Robotics and Automation (ICRA 2024)
May 13-17, 2024. Yokohama, Japan

Achieving Mechanical Transparency Using Fusion Hybrid Linear Actuator for Shoulder Flexion and Extension in Exoskeleton Robot

Takuma SHIMOYAMA[1,2], Tomoyuki NODA[2,1], Tatsuya TERAMAE[2], and Yoshihiro NAKATA[1*]

***Abstract*— Recently, the importance of mechanical transparency in human-assistive robots has grown. Traditionally, its primary goal was minimizing interaction forces during assistance. However, under this conventional definition, mechanical transparency was not considered when an interaction force was required during assistance. This research focuses on achieving mechanical transparency within the context of shoulder motion in upper extremity exoskeletons for rehabilitation. Our primary goal is maintaining interaction forces at target values, even with motion disturbances. To this end, we developed a shoulder actuation testbed for exoskeletons, incorporating a fusion hybrid linear actuator distinguished by high back-drivability, robust torque generation capability, and safety features. To attain mechanical transparency, we created a model for calculating the required joint torque, accounting for gravitational dynamics, and subsequently determined the necessary actuator output. The system characteristics were evaluated based on the joint torque generated by the actuator. The actuator utilized pneumatic pressure to generate force and compensated for kinetic friction using electromagnetic forces. The results showed that the compensation by the electromagnetic force reduced the root mean square error of the torque to less than 60% in relation to pneumatic pressure alone. This demonstrated the ability to generate consistent torque with high robustness to motion disturbances.**

I. Introduction

Stroke, the second leading cause of death worldwide, affects more than 12 million people annually, and more than half succumb to it [1][2]. Stroke survivors often experience adverse effects. Approximately 70% of post-stroke patients experience impaired arm function, with hemiplegia being the most common sequela [3]. Several guidelines recommend early and repeated rehabilitation for hemiplegia considering the plasticity of the brain in neurorehabilitation [3][4]. However, for reasons such as a shortage of therapists and difficulties in securing treatment time, it is challenging for patients to receive adequate rehabilitation. Therefore, there is potential for patients to perform high-quality rehabilitation on their own by using rehabilitation robots, thus addressing the need for repetitive therapy.

*This work was supported by JSPS KAKENHI Grant Number JP21H04911 (development and experiments with the actuator and the shoulder actuation testbed), and JST Moonshot R&D Grant Number JPMJMS2034 (development of the pneumatic control interface).

[1]Department of Mechanical and Intelligent Systems Engineering, Graduate School of Informatics and Engineering, The University of Electro-Communications, Chofu, Tokyo, Japan. {tshimoyama, ynakata}@uec.ac.jp

[2]Department of Brain Robot Interface, ATR Computational Neuroscience Laboratories, Soraku-gun, Kyoto, Japan. {t_noda, t-teramae}@atr.jp

*Y. Nakata is the corresponding author. ynakata@uec.ac.jp

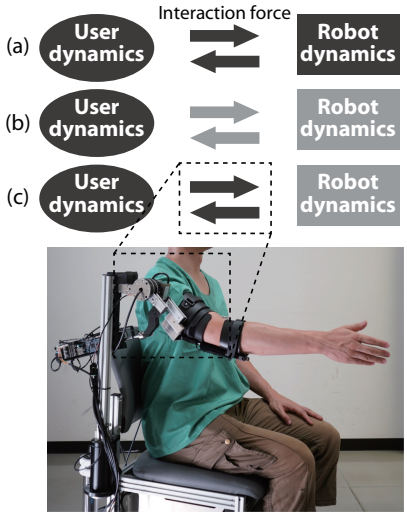

Fig. 1: Concept of 'transparency' in human-assistive rehabilitation robots: (a) Conventional robot: The robot's inherent dynamics constrain the user's movement. (b) Conventional transparency concept: Interaction force between the robot and the user is zero, suggesting no physical assistance. (c) Proposed transparency concept for essential human-assistance: Despite the presence of an interaction force indicating assistance, the robot's inherent dynamics do not constrain the user's movement.

Shoulder rehabilitation is essential for supporting the full weight of the upper extremities during hand movements to perform activities of daily living. In addition, several studies have demonstrated the effectiveness of patient-driven control [5], where robots support the patient's voluntary movements, in the control strategy of rehabilitation robots. T-Wrex [6] or L-Exos [7] have demonstrated the effectiveness of supporting for the patient's arm weight, while ARMin [8] has demonstrated the benefits of intensive rehabilitation by switching between robot- and patient-initiated control, and BONES [9] or Pneu-Wrex [10] have demonstrated the effectiveness of assist-as-needed control strategies, which assist with the required amount of force. Furthermore, the safety of the robot–patient interaction should be of particular concern considering that patients have reduced motor function in relation to healthy individuals [11]. Therefore, inherent back-drivability is essential. In this study, we aimed to achieve a high output torque to support the upper limb under gravity compensation and a robust output torque against motion disturbances while maintaining intrinsic back-drivability.

Fig. 1(a)–1(c) illustrates the concept of 'transparency' in human-assistive rehabilitation robots. As shown in Fig. 1(a), a conventional challenge in assistive robots is the impact of the robot's inherent dynamics on a user when wearing a robot. As shown in Fig. 1(b), conventional mechanical transparency is a concept in which a robot does not affect the user as if it were transparent. Previous research evaluated this mechanical transparency by setting the interaction force between the robot and wearer to zero. However, the mechanical transparency when rehabilitation robots assist the wearer's movements has not been thoroughly investigated. In other words, mechanical transparency during the generation of assistive forces by the drive system of a robot has not been sufficiently discussed. As shown in Fig. 1(c), our research fundamentally focuses on generating interaction forces while ensuring that the dynamics of the robot do not constrain the user's movement.

The previously developed integrated pneumatic–electromagnetic hybrid linear actuator (iPEHLA) [12], which is a realization of the innovative concept of fusion hybrid linear actuator [13], outputs the base force by pneumatic force and compensates for mechanical losses using an electromagnetic force, enabling increased precision of force control. iPEHLA achieves high back-drivability by fusing two direct-drive linear actuators, that is, an air cylinder and a linear motor. It has been demonstrated that iPEHLA can maintain a constant force against motion disturbances affecting the mover by compensating for kinetic friction in the cylinder with electromagnetic forces. However, as iPEHLA is a linear actuator, its application to rotary-drive joints is not a trivial problem. In this study, we developed a shoulder actuation testbed for exoskeletons using iPEHLA to achieve a robust torque output in the joint against motion disturbances.

1) We expanded the conventional definition of mechanical transparency and focused on a new concept where the interaction force is maintained as desired even under motion disturbances.
2) A shoulder actuation testbed driven by a fusion hybrid actuator was developed for an exoskeleton for flexion and extension rehabilitation.
3) A torque generation model for the testbed was created.
4) An experimental setup and evaluation system were developed to evaluate the characteristics of the test bed in response to motion disturbances, and the accuracy of force control between the pneumatic-only force control and force control combining pneumatic and electromagnetic forces was compared.

II. Shoulder Actuation Testbed for Exoskeleton

This section introduces the concept and design of the testbed and the process of deriving the torque generation model.

A. Concept

This study developed a shoulder actuation testbed for the exoskeleton. The shoulder actuation testbed for the exoskeleton comprised a shoulder joint mechanism and its driving actuator designed for the rehabilitation of flexion and extension motions in upper extremity exoskeletons. The testbed was designed to provide sufficient torque to lift the upper arm, achieve robust torque against motion disturbances, and be inherently safe to operate without mechanical constraints.

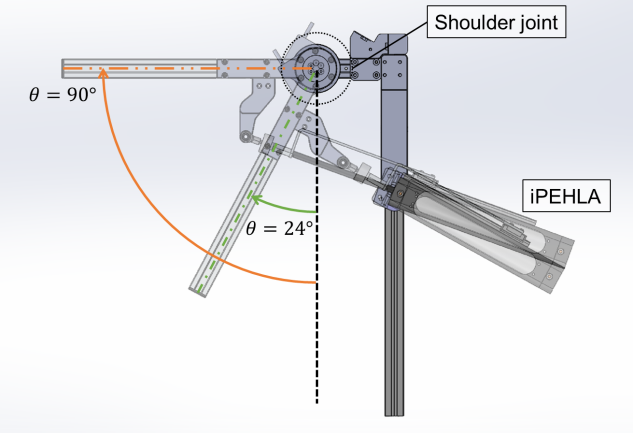

Fig. 2: Motion range of the shoulder joint mechanism.

Co-author Noda has previously proposed several pneumatically driven exoskeletons, and although they achieved inherent back-drivability using pneumatic systems, their torque control performance was insufficient. In the exoskeleton that uses an air cylinder [14] to provide sufficient torque and safety, force hysteresis owing to kinetic friction between the cylinder and piston makes it difficult to generate a robust force against motion disturbances. Furthermore, an exoskeleton mechanism employing a hybrid pneumatic–electric drive to compensate for the pneumatic artificial muscle output using geared motors was developed [15]. This exoskeleton achieves consistent back-drivability by setting a lower gear-reduction ratio for the motors. However, this comes with the challenge of complex transmission mechanisms required to synthesize torque. iPEHLA has the potential to address these issues by synthesizing pneumatic and electromagnetic forces while maintaining high back-drivability without the use of a reduction gear.

B. Design

Fig. 2 shows the testbed in action. The fixed portion of iPEHLA rotates freely on the vertical plane according to the angle of the arm. This angle is limited to $\theta = 90°$, which corresponds to the horizontal plane, by a physical lock in the shoulder joint.

Fig. 3 shows the structure of the iPEHLA used in the testbed developed in this study. iPEHLA has an integrated structure in which the pneumatic and electromagnetic actuators share moving parts (piston and permanent magnet array) and moving spaces (cylinder and winding). Because iPEHLA does not use mechanical elements for force synthesis, there is little energy loss, and it has inherent back-drivability. Its volume is smaller than the sum of an air cylinder and an electromagnetic actuator, making it easy to mount on a robot.

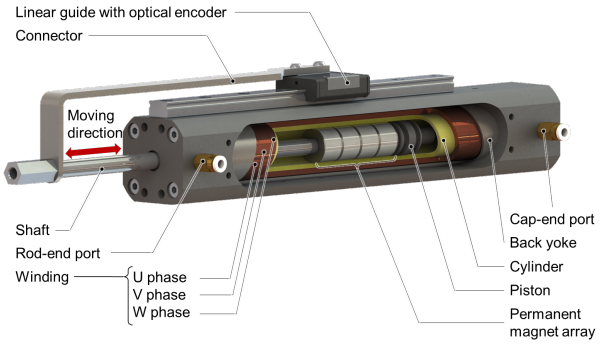

Fig. 3: Structure of iPEHLA. The part of the model is sectioned.

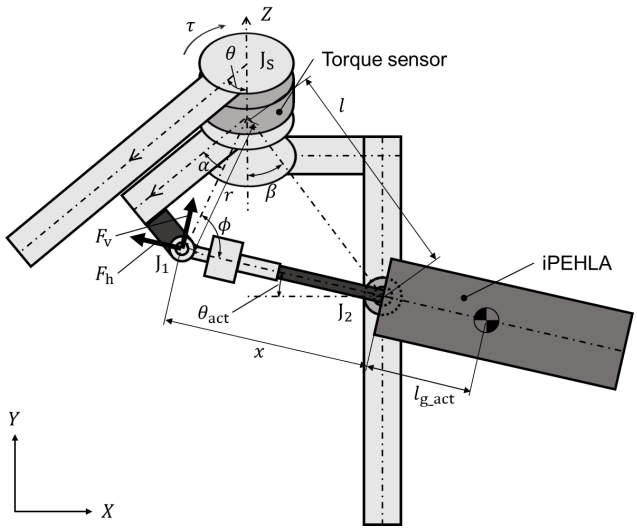

Fig. 4: Schematic of the testbed.

iPEHLA outputs the base force using pneumatic force and compensates for the output using the electromagnetic force.

iPEHLA, previously reported by co-authors Nakata et al., was realized by modifying a commercially available actuator. On the other hand, the actuator used in this study was newly designed and prototyped. The mover configuration was also optimized because the motion range of iPEHLA is limited by the permanent magnet attached to the shaft. Building upon the foundation of a previous design [13], we halved the number of permanent magnets from eight to four. This reduction was strategically chosen to expand the actuator's range of motion while still retaining adequate electromagnetic force for friction compensation. Since the number of magnets was halved, the electromagnetic force constant was treated as 4.0 N/A, which is half of the 8.02 N/A of the previous model [13]. Furthermore, machine-wound coils were used to improve the number of turns and reduce manufacturing issues when the coils were hand-wound.

C. Control

1) Torque Generation Model: Fig. 4 shows the testbed schematic and parameters. The testbed had three joints; J_s was the shoulder joint, and J_1 and J_2 mounted iPEHLA on the testbed. The shoulder joint J_s was structured in two stages, with a torque sensor placed between the upper and lower aluminum frames. iPEHLA was connected to the lower frame by the joint J_1, and the human arm was in contact with the upper frame. iPEHLA was mounted to the frame at joint J_2 and was free to rotate to match the angle of the arm. Table I summarizes the parameters of the testbed. The equations of motion of the robot can be expressed as

TABLE I: Parameters of the testbed.

Symbol	Description	Value
m_{mover}	iPEHLA mover mass	0.144 kg
m_{stator}	iPEHLA stator mass	0.751 kg
s	Contact area between sealing fin and cylinder	20.6 mm^2
α	Angle of testbed's shape	44°
β	Angle of testbed's shape	33°
r	Distance between J_s and J_1	128 mm
l	Distance between J_s and J_2	190 mm
l_{piston}	Distance between J_1 and center of piston	257 mm

$$I_{\text{arm}}\ddot{\theta} + \tau_{\text{g\_arm}}(\theta) = \tau_{\text{int}} + \tau_{\text{Js}} \tag{1}$$

where I_{arm} is the moment of inertia around the shoulder joint of the robot arm, $\tau_{\text{g\_arm}}$ is the torque around the shoulder joint due to gravity on the upper frame, τ_{int} is the interaction torque between the human and robot arms, and τ_{Js} is the output torque of the robot's shoulder joint. The friction of the rotating bearings was neglected in this model. τ_{Js} is represented by equation (2). In this study, we aimed to keep it constant under motion disturbances.

$$\tau_{\text{Js}} = r\left(F_{\text{h}}\sin\phi + F_{\text{v}}\cos\phi\right) + \tau_{\text{g\_Js}}(\theta) + \tau_{\text{I\_Js}}(\ddot{\theta}) \tag{2}$$

where r is the distance between J_s and J_1, F_{h} is the force that iPEHLA exerts on J_1 along the shaft advancing direction, F_{v} is the force that iPEHLA exerts on J_1 perpendicular to the shaft direction, and $\tau_{\text{g\_Js}}$ and $\tau_{\text{I\_Js}}$ are the torque around the shoulder joint due to gravity and inertia on the lower frame, respectively. ϕ can be expressed as

$$\phi(\theta) = \arccos\frac{r - l\cos\left(\theta - \alpha + \beta\right)}{\sqrt{r^2 + l^2 - 2rl\cos\left(\theta - \alpha + \beta\right)}} \tag{3}$$

where l is the distance between J_s and J_2, and α and β are the angles shown in Fig. 4.

F_{v} can be expressed as

$$F_{\text{v}} = F_{\text{g\_act}} - \frac{I_{\text{act}}\ddot{\theta}_{\text{act}}}{x} \tag{4}$$

where $F_{\text{g\_act}}$ is the component of F_{v} due to gravity on iPEHLA, I_{act} is the moment of inertia around the J_2 joint of iPEHLA, and θ_{act} is the angle of iPEHLA. $F_{\text{g\_act}}$ can be expressed as

$$\begin{aligned} F_{\text{g\_act}}(\theta) =& \frac{l_{\text{g\_act}}(x)}{x}\left(m_{\text{stator}} + m_{\text{mover}}\right) g\cos\left(\theta_{\text{act}}\right) \\ \text{where} \quad & \theta_{\text{act}}(\theta) = \theta + \phi - \alpha - \frac{\pi}{2} \end{aligned} \tag{5}$$

where x is the distance between J_s and J_1, $l_{\text{g\_act}}$ is the distance

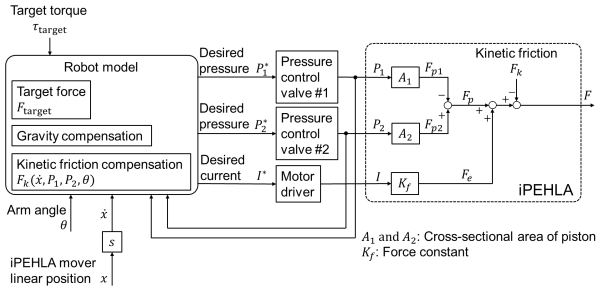

Fig. 5: Block diagram of the testbed system.

TABLE II: Parameters of the kinetic friction model.

Symbol	Description	Value
μ_S	Static friction coefficient	0.272
μ_C	Coulomb friction coefficient	0.170
F_0	Contact force of the moving part to the stator at $P_1 = P_2 = 0$ and $F_v = 0$	14.3 N
v_s	Stribeck velocity	0.00132 m/s
σ_2	Viscous friction coefficient	0.00 Ns/m

between J_1 and the iPEHLA center of gravity, and m_{stator} and m_{mover} are the stator and mover masses, respectively.

F_h can be expressed as

$$F_h = F_p + F_e - F_k - m_{mover}\ddot{x} - m_{mover} g \sin(\theta_{act}) \quad (6)$$

where F_p and F_e are the pneumatic and electromagnetic outputs, and F_k is the kinetic friction force occurring at the contact area between the mover and stator.

2) Kinetic Friction Model: The mover and stator were fluid-lubricated with silicon grease. The kinetic friction model, F_k, considering the Stribeck effect proposed by Canudas de Wit et al. [16] is expressed as

$$F_k = F_C \mathrm{sgn}(\dot{x}) + (F_S - F_C) e^{-(\dot{x}/v_s)^2} \mathrm{sgn}(\dot{x}) + \sigma_2 \dot{x} \quad (7)$$

where F_C is the Coulomb friction force, F_S is the static friction force, v_s is the Stribeck velocity, and σ_2 is the viscous friction coefficient. Co-authors Nakata et al. [13] re-modeled the kinetic friction by considering the change in the contact force of the sealing fin on the cylinder owing to the change in the pressure in the cylinder.

$$\begin{aligned} F_k(\dot{x}, P) = {} & \mu_C (s \cdot P + F_0) \mathrm{sgn}(\dot{x}) \\ & + (\mu_S - \mu_C)(s \cdot P + F_0) e^{-(\dot{x}/v_s)^2} \mathrm{sgn}(\dot{x}) \\ & + \sigma_2 \dot{x} \end{aligned} \quad (8)$$

where μ_C and μ_S are the Coulomb and static friction coefficients, respectively, s is the contact area between the sealing fin and cylinder, and F_0 is the contact force of the mover to the stator at $P = 0$ (atmosphere condition).

Because air chambers on both sides of the iPEHLA were used in this testbed, it was necessary to consider the changes in the contact force of the sealing fins to the cylinder owing to the changes in the air pressure on both sides. In addition, the contact force between the mover and stator increased owing to the support reaction force of F_v. Assuming that the shaft is simply supported at two points, the piston-cylinder

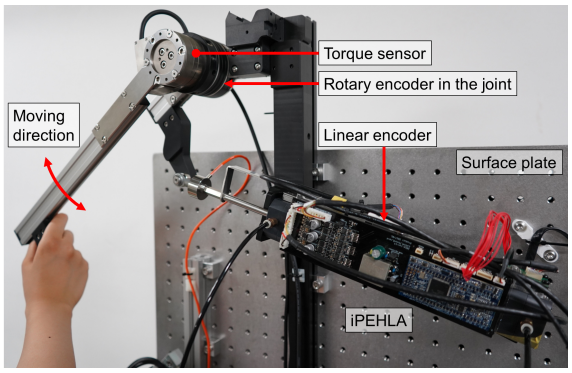

Fig. 6: Photograph of the experimental setup.

and shaft-packing, (8) can be re-written as

$$\begin{aligned} F_k(\dot{x}, P_1, P_2, \theta) = {} & \mu_C F_{contact} \mathrm{sgn}(\dot{x}) \\ & + (\mu_S - \mu_C) F_{contact} e^{-(\dot{x}/v_s)^2} \mathrm{sgn}(\dot{x}) \\ & + \sigma_2 \dot{x} \\ \text{where } F_{contact} = {} & s \cdot (P_1 + P_2) + F_0 + F_{v1} + F_{v2} \\ F_{v1} = {} & \{l_{piston}/(l_{piston} - x)\} F_v \\ F_{v2} = {} & \{x/(l_{piston} - x)\} F_v \end{aligned} \quad (9)$$

where P_1 and P_2 are the pressure of the air chamber on the rod- and the cap-end port sides (Fig. 2), respectively. F_0 is the contact force of the moving part to the stator at $P_1 = P_2 = 0$ and $F_v = 0$. F_{v1} and F_{v2} are the support reaction forces of F_v acting between the shaft and packing and between the piston and cylinder, respectively. Fig. 5 shows the block diagram of the testbed system. Table II summarizes the parameters of the kinetic friction model.

III. EXPERIMENTS

Among the definitions of mechanical transparency proposed in this study, we evaluated the performance of the testbed when the target value of the interaction force was constant. The capability of the testbed to maintain a constant torque output against motion disturbances was compared for several conditions and control methods.

A. Experimental Setup

Fig. 6 shows the experimental setup. The testbed of the robot was fixed to a vertically standing optical surface plate, and the robot's arm was manually driven to the beat of a metronome. Fig. 7 shows the configuration of the experimental setup. The shoulder joint angle was measured by using an optical encoder (AEDR-871x, Broadcom Inc.). The output torque was measured using a torque sensor (PFS055YA251R6, Leptrino Co., Ltd.) attached to the joint. The position of the iPEHLA moving part was measured using a optical encoder (AEDR-871x, Broadcom Inc.). Air pressure was supplied to the iPEHLA cylinder after reducing the air pressure from the compressor (SRL-A3.7DVA, Hitachi, Ltd.) using a regulator (IR2020-02BG-R, SMC Corp.), and the pressure was controlled using a pressure control valve (VP5010SBJ111H00, Norgren Inc.). The data from each

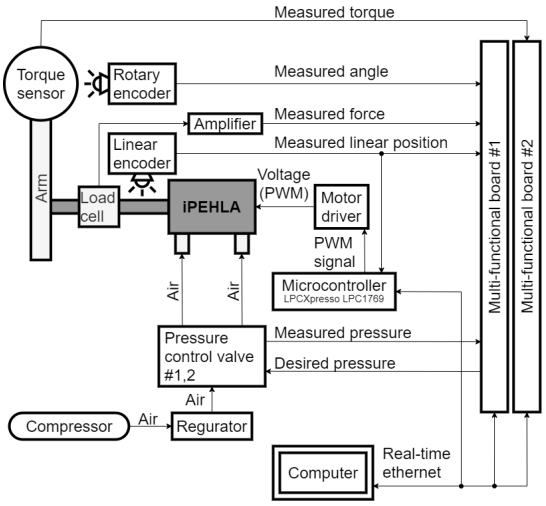

Fig. 7: System configuration of the experimental setup. Some values were not used in this experiment and analysis.

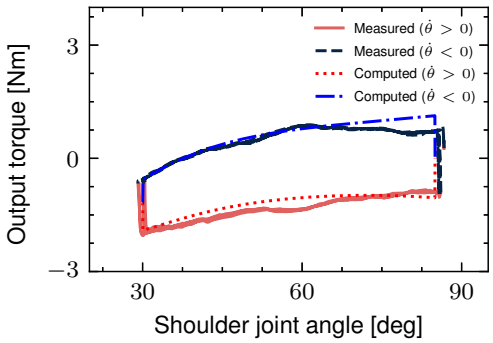

Fig. 8: Comparison between calculated and measured torque.

sensor were recorded on a computer using multi-functional boards.

B. Model Validation

The torque computed according to the model was compared with the measured torque. In the calculations, the shoulder joint angular velocity was treated as a constant of 0.25 rad/s, while angular acceleration $\ddot{\theta}, \ddot{\theta}_{\text{act}}$, and iPEHLA mover acceleration $\ddot{x}$ were assumed to be 0. Additionally, the measurements were performed in the range of $30° \leq \theta \leq 85°$, with a target angular velocity of 0.25 rad/s, and a total of 5 cycles were performed.

Fig. 8 shows a comparison of the calculated and measured torques. The calculated and measured torques were approximately in agreement, but a discrepancy was observed in the range of about $\theta > 65°$.

C. Evaluation of Output Torque Robustness

We evaluated the output torque when compensation for the output was performed based on the model validated in Section III-B. The joint angular velocity was set at two conditions: slow-condition (target 0.25 rad/s) and fast-condition (target 0.5 rad/s). The target output torque was set at three conditions: 0 Nm, 3 Nm, and 6 Nm. These conditions

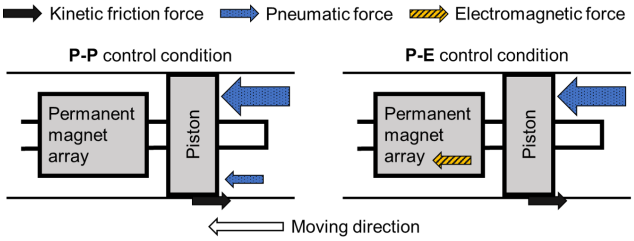

Fig. 9: Comparison of control conditions for iPEHLA.

TABLE III: Mean RMSE and mean angular velocity

Conditions	Slow, P–P	Slow, P–E	Fast, P–P	Fast, P–E
Mean RMSE [Nm]	0.27	0.16	0.58	0.32
Mean angular velocity [rad/s]	0.31	0.31	0.65	0.66

were determined based on empirical knowledge considering rehabilitation for moderate hemiplegia Japanese individuals with standard body shapes.

Two iPEHLA control conditions were established: P–P and P–E (Fig. 9).

P–P The base force was generated by air pressure, and the kinetic friction was compensated by air pressure. P–P (Pneumatic base force – Pneumatic compensation force) control is achievable using conventional air cylinders.

P–E The base force was generated by air pressure, and the kinetic friction was compensated by electromagnetic force. P–E (Pneumatic base force – Electromagnetic compensation force) control is achievable only with iPEHLA.

The base force, F_{base}, was derived from equations (2), (4) and (6) as follows:

$$F_{\text{base}} = m_{\text{mover}}\ddot{x} + m_{\text{mover}}g\sin(\theta_{\text{act}}) + \{\tau_{\text{Js\_target}} - r(F_{\text{g\_act}} - \frac{I_{\text{act}}\ddot{\theta}_{\text{act}}}{x})\cos\phi - \tau_{\text{g\_Js}} - \tau_{\text{l\_Js}}\}/r\sin\phi \quad (10)$$

where $\tau_{\text{Js\_target}}$ is the desired torque. In our experiment, the inertia of the testbed ($I_{\text{act}}\ddot{\theta}_{\text{act}}/x$, $m_{\text{mover}}\ddot{x}$, and $\tau_{\text{l\_Js}}$) and gravitational force of the iPEHLA mover along the shaft direction ($m_{\text{mover}}g\sin(\theta_{\text{act}})$) were ignored because they were very small.

For a total of 12 conditions, measurements were performed in the range of $30° \leq \theta \leq 85°$, and 5 cycles were performed under each condition.

D. Results

Fig. 10(a) shows the output torque under the slow-condition and Fig. 10(b) shows the output torque under the fast-condition. In this study, we did not consider the static friction force between the iPEHLA mover and stator, which resulted in peaks at both ends of the torque loop. Moreover, the root mean square error (RMSE) of the output torque from the target torque for each condition and direction of movement is shown in Fig. 10(c). However, to assess the

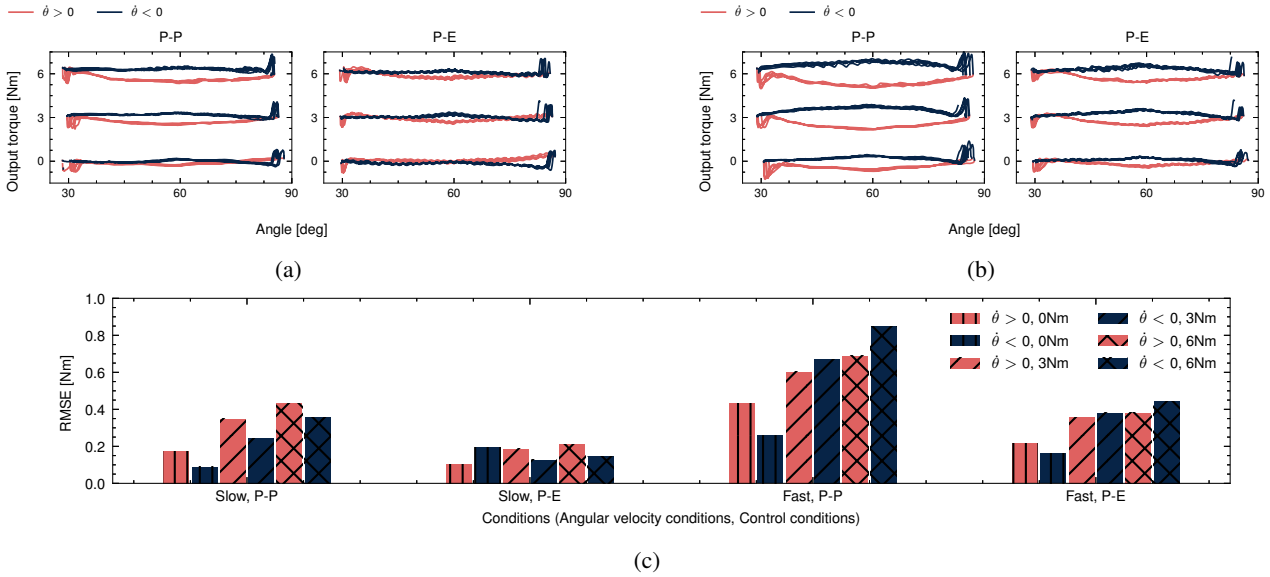

Fig. 10: Results of the experiments. (a) Output torque under the slow-condition. (b) Output torque under the fast-condition. (c) Comparison of RMSE of the torque under different conditions.

dynamic state excluding the influence of peaks, the RMSE was calculated within the range of $35^\circ \leq \theta \leq 80^\circ$.

The RMSE of the output torque tended to increase with an increase in the angular velocity or target torque. The mean values of the RMSE and angular velocity for each angular velocity and control condition are presented in Table III. The average RMSE under the P–E condition was smaller than that under the P–P condition in both the slow- and fast-conditions.

IV. DISCUSSION

The ratio of the average RMSE for the P–E control condition to that of the P–P control condition (only air utilized for actuation) was 59% for the slow-condition and 55% for the fast-condition. This demonstrates the effectiveness of friction compensation by electromagnetic force, especially at higher angular velocities. Driving a rehabilitation robot with iPEHLA is expected to improve the mechanical transparency of the robot during assistance by maintaining torque at the target value against motion disturbances while maintaining inherent back-drivability.

Even in the P–E condition, some deviations from the target torque remained. This is probably because, in this study, only kinetic friction compensation was performed using electromagnetic forces, and the compensation of pneumatic output delay for gravity compensation and target torque generation was not considered. It is expected that by modeling the pneumatic delay and considering the valve characteristics and compressibility of air, the torque deviation in P–E control can be further reduced.

The average angular velocity under the slow-condition was 0.31 rad/s for the P–P condition and 0.31 rad/s for the P–E condition, showing almost no difference between them. The average angular velocity under the fast-condition was 0.65 rad/s for the P–P condition and 0.66 rad/s for the P–E condition, confirming a small difference between the two. In this experiment, motion disturbances were manually applied to the upper frame. However, there were no significant problems when the results for each condition were compared.

Comparing the calculated and measured torque for the validation of the model, a discrepancy in the range of about $\theta > 65^\circ$ was observed. This occasionally resulted in excessive kinetic friction compensation, as shown in Fig. 10(a) or Fig. 10(b). It is possible that for a large range of θ, that is, when x is large, the value of the force applied to the piston, F_{v2}, becomes significant, potentially causing deformation in the piston and changing the model. In addition, as the force applied to the packing, F_{v1} increased, there was a possibility that the packing deformed, causing changes to the model. The relationship between the forces acting perpendicular to the iPEHLA shaft and the kinetic friction model requires more detailed investigation in the future.

V. CONCLUSIONS

We focused on a new concept of mechanical transparency in which the interaction force is maintained as desired, even under motion disturbances. In addition, a shoulder actuation testbed was developed for an exoskeleton for shoulder flexion and extension rehabilitation. It was equipped with iPEHLA, a fusion hybrid actuator that synthesizes pneumatic and electromagnetic forces. Furthermore, a model of the drive joint was created and validated, and the robustness of the output torque to motion disturbances was investigated when gravity and kinetic friction were compensated according to the model. The experimental results suggested that friction compensation by electromagnetic forces may increase the robustness of the output to motion disturbances, making the rehabilitation robot more transparent.

We will soon conduct a clinical trial in a hospital setting after a detailed study of the model and a review of the electromagnetic force compensation intervention.

REFERENCES

[1] GBD 2019 Stroke Collaborators, "Global, regional, and national burden of stroke and its risk factors, 1990-2019: a systematic analysis for the global burden of disease study 2019," *The Lancet Neurology*, vol. 20, no. 10, pp. 795–820, Oct 2021. [Online]. Available: https://doi.org/10.1016/S1474-4422(21)00252-0

[2] V. L. Feigin, M. Brainin, B. Norrving, S. Martins, R. L. Sacco, W. Hacke, M. Fisher, J. Pandian, and P. Lindsay, "World stroke organization (wso): Global stroke fact sheet 2022," *International Journal of Stroke*, vol. 17, no. 1, pp. 18–29, 2022, pMID: 34986727. [Online]. Available: https://doi.org/10.1177/17474930211065917

[3] Royal College of Physicians, *National Clinical Guidelines for Stroke*. Royal College of Physicians, 2023.

[4] C. J. Winstein, J. Stein, R. Arena, B. Bates, L. R. Cherney, S. C. Cramer, F. Deruyter, J. J. Eng, B. Fisher, R. L. Harvey, C. E. Lang, M. MacKay-Lyons, K. J. Ottenbacher, S. Pugh, M. J. Reeves, L. G. Richards, W. Stiers, and R. D. Zorowitz, "Guidelines for adult stroke rehabilitation and recovery," *Stroke*, vol. 47, no. 6, pp. e98–e169, 2016. [Online]. Available: https://www.ahajournals.org/doi/abs/10.1161/STR.0000000000000098

[5] N. Rehmat, J. Zuo, W. Meng, Q. Liu, S. Q. Xie, and H. Liang, "Upper limb rehabilitation using robotic exoskeleton systems: a systematic review," *International Journal of Intelligent Robotics and Applications*, vol. 2, no. 3, pp. 283–295, Sep 2018. [Online]. Available: https://doi.org/10.1007/s41315-018-0064-8

[6] S. J. Housman, K. M. Scott, and D. J. Reinkensmeyer, "A randomized controlled trial of gravity-supported, computer-enhanced arm exercise for individuals with severe hemiparesis," *Neurorehabilitation and Neural Repair*, vol. 23, no. 5, pp. 505–514, 2009, pMID: 19237734. [Online]. Available: https://doi.org/10.1177/1545968308331148

[7] A. Frisoli, C. Procopio, C. Chisari, I. Creatini, L. Bonfiglio, M. Bergamasco, B. Rossi, and M. C. Carboncini, "Positive effects of robotic exoskeleton training of upper limb reaching movements after stroke," *Journal of NeuroEngineering and Rehabilitation*, vol. 9, no. 1, p. 36, Jun 2012.

[8] P. Staubli, T. Nef, V. Klamroth-Marganska, and R. Riener, "Effects of intensive arm training with the rehabilitation robot armin ii in chronic stroke patients: four single-cases," *Journal of NeuroEngineering and Rehabilitation*, vol. 6, no. 1, p. 46, Dec 2009. [Online]. Available: https://doi.org/10.1186/1743-0003-6-46

[9] M.-H. Milot, S. J. Spencer, V. Chan, J. P. Allington, J. Klein, C. Chou, J. E. Bobrow, S. C. Cramer, and D. J. Reinkensmeyer, "A crossover pilot study evaluating the functional outcomes of two different types of robotic movement training in chronic stroke survivors using the arm exoskeleton bones," *Journal of NeuroEngineering and Rehabilitation*, vol. 10, no. 1, p. 112, Dec 2013. [Online]. Available: https://doi.org/10.1186/1743-0003-10-112

[10] D. J. Reinkensmeyer, E. T. Wolbrecht, V. Chan, C. Chou, S. C. Cramer, and J. E. Bobrow, "Comparison of three-dimensional, assist-as-needed robotic arm/hand movement training provided with pneu-WREX to conventional tabletop therapy after chronic stroke," *American Journal of Physical Medicine & Rehabilitation*, vol. 91, no. 11, pp. S232–S241, Nov. 2012. [Online]. Available: https://doi.org/10.1097/phm.0b013e31826bce79

[11] R. Morales, F. J. Badesa, N. García-Aracil, J. M. Sabater, and C. Pérez-Vidal, "Pneumatic robotic systems for upper limb rehabilitation," *Medical & Biological Engineering & Computing*, vol. 49, no. 10, pp. 1145–1156, Oct 2011. [Online]. Available: https://doi.org/10.1007/s11517-011-0814-3

[12] Y. Nakata, T. Noda, J. Morimoto, and H. Ishiguro, "Development of a pneumatic-electromagnetic hybrid linear actuator with an integrated structure," in *2015 IEEE/RSJ International Conference on Intelligent Robots and Systems (IROS)*, 2015, pp. 6238–6243.

[13] Y. Nakata and T. Noda, "Fusion hybrid linear actuator: Concept and disturbance resistance evaluation," *IEEE/ASME Transactions on Mechatronics*, vol. 28, no. 4, pp. 2167–2177, 2023.

[14] T. Noda and J. Morimoto, "Development of upper-extremity exoskeleton driven by pneumatic cylinder toward robotic rehabilitation platform for shoulder elevation," in *2015 IEEE International Conference on Rehabilitation Robotics (ICORR)*, 2015, pp. 496–501.

[15] T. Noda, T. Teramae, B. Ugurlu, and J. Morimoto, "Development of an upper limb exoskeleton powered via pneumatic electric hybrid actuators with bowden cable," in *2014 IEEE/RSJ International Conference on Intelligent Robots and Systems*, 2014, pp. 3573–3578.

[16] C. Canudas de Wit, H. Olsson, K. Astrom, and P. Lischinsky, "A new model for control of systems with friction," *IEEE Transactions on Automatic Control*, vol. 40, no. 3, pp. 419–425, 1995.